Nuclear transport receptor binding avidity triggers a self-healing collapse transition in FG-nucleoporin molecular brushes

Rafael L. Schoch, Larisa E. Kapinos, and Roderick Y. H. Lim[1]

Biozentrum and Swiss Nanoscience Institute, University of Basel, 4056 Basel, Switzerland

Edited by* Günter Blobel, The Rockefeller University, New York, NY, and approved September 4, 2012 (received for review May 18, 2012)

Conformational changes at supramolecular interfaces are fundamentally coupled to binding activity, yet it remains a challenge to probe this relationship directly. Within the nuclear pore complex, this underlies how transport receptors known as karyopherins proceed through a tethered layer of intrinsically disordered nucleoporin domains containing Phe-Gly (FG)-rich repeats (FG domains) that otherwise hinder passive transport. Here, we use nonspecific proteins (i.e., BSA) as innate molecular probes to explore FG domain conformational changes by surface plasmon resonance. This mathematically diminishes the surface plasmon resonance refractive index constraint, thereby providing the means to acquire and correlate height changes in a surface-tethered FG domain layer to Kap binding affinities in situ with respect to their relative spatial arrangements. Stepwise measurements show that FG domain collapse is caused by karyopherin β1 (Kapβ1) binding at low concentrations, but this gradually transitions into a reextension at higher Kapβ1 concentrations. This ability to self-heal is intimately coupled to Kapβ1-FG binding avidity that promotes the maximal incorporation of Kapβ1 into the FG domain layer. Further increasing Kapβ1 to physiological concentrations leads to a "pileup" of Kapβ1 molecules that bind weakly to unoccupied FG repeats at the top of the layer. Therefore, binding avidity does not hinder fast transport per se. Revealing the biophysical basis underlying the form–function relationship of Kapβ1-FG domain behavior results in a convergent picture in which transport and mechanistic aspects of nuclear pore complex functionality are reconciled.

biointerface | molecular crowding | multivalent binding | nucleocytoplasmic transport | polymer brush

Intrinsically disordered proteins (IDPs) that adorn the surfaces of biomolecular structures are thought to confer a host of unique functionalities not found in structured proteins (1). However, unlike their free-floating counterparts in solution (2), the properties of such surface-tethered IDPs can be particularly challenging to evaluate because of their inherent flexibility and conformational susceptibility to local interfacial constraints (3). Herein lies the crux of the nuclear pore complex (NPC) problem, in which in vitro efforts (4–11) to rationalize the collective form–function characteristics of the intrinsically disordered Phe-Gly (FG) domains (12) typically neglect the uncertainty regarding their numbers [approximately 200 divided amongst 11 different FG-bearing nucleoporins (Nups) (13)], their locations within the central NPC channel, and corresponding distances between neighboring anchoring sites (14). As the key components of the NPC barrier mechanism, the manner by which the FG domains impede nonspecific molecules (greater than 40 kDa) whilst granting karyopherins (Kaps) and their cargoes access between the nucleus and the cytoplasm (15–17) is likely to be influenced by such physical constraints. Accordingly, it remains unaccounted for how these contextual details can influence (*i*) FG domain barrier conformation, (*ii*) Kap-FG binding avidity (18) [i.e., Kapβ1, also known as importinβ or impβ, has an estimated 10 FG binding sites (19, 20)], and (*iii*) subsequent binding-induced conformational changes in the FG domains (21).

As Paine et al. wrote in 1975, "as solute size approaches the dimensions of the (nuclear) pore, solute–pore wall interactions become increasingly important. Specific site interactions…would also influence solute movements" (22). Yet, the sheer molecular complexity of the NPC (23) has for the most part motivated reductionist approaches to tease apart FG domain function in vitro (4–11). Not surprisingly, inherent differences in experimental approach and length scale that largely overlook such "solute–pore wall interactions" have led to differing views on the matter. Briefly, the selective phase model (5, 8) derives from the characteristics of macroscopic FG hydrogels whereby the FG domains form a "self-healing" sieve-like meshwork that only Kaps can dissolve through. The polymer brush model (4) is based on nanoscale validation of how surface-tethered FG domains entropically exclude nonspecific cargoes (24) whilst promoting Kap access by reversibly collapsing (6). On this basis, it has been postulated that permanently collapsed FG domains at physiological Kap concentrations might provide a hydrophobic "FG-rich layer" around the NPC walls for the surface diffusion of Kap-cargo complexes—i.e., "reduction of dimensionality" (25). Finally, the trees and brushes model (26) proposes that a bimodal distribution of collapsed and extended FG domain regions within the NPC provides distinct transport routes for Kap-cargo complexes and passive diffusion, respectively. To add to the confusion, mechanistic and kinetic views of NPC transport also appear to be at odds. One example pertains to the collapse of Nup153 FG domain brushes upon binding Kapβ1 at picomolar concentrations (6), which has been interpreted (10) to imply a substantially stronger binding affinity over reported K_D values (approximately 10 nM) (27). Indeed, the incompatibility of in vitro–obtained Kapβ1-FG domain binding affinities (27–29) to describe in vivo transport rates questions even the relevance of known K_D measurements (30).

In this work, we sought to correlate the conformational changes of surface-tethered FG domains directly to multivalent Kapβ1-FG binding interactions (i.e., binding avidity) using a surface plasmon resonance (SPR)-based assay that we developed for this purpose. Importantly, this allows for an in situ measure of FG domain surface density, conformational height change, and Kap-FG binding activity. As an analytical biosensing technique, SPR monitors the change in the angle of incidence light required to create surface plasmon resonance as molecular binding events occur in real time in proximity to the glass/metal sensor surface (31–33). In this way, rate and equilibrium constants are

Author contributions: R.L.S., L.E.K., and R.Y.H.L. designed research; R.L.S. and L.E.K. performed research; R.L.S. and L.E.K. contributed new reagents/analytic tools; R.L.S., L.E.K., and R.Y.H.L. analyzed data; and R.L.S., L.E.K., and R.Y.H.L. wrote the paper.

The authors declare no conflict of interest.

*This Direct Submission article had a prearranged editor.

[1]To whom correspondence should be addressed. E-mail: roderick.lim@unibas.ch.

This article contains supporting information online at www.pnas.org/lookup/suppl/doi:10.1073/pnas.1208440109/-/DCSupplemental.

determined as analytes from solution bind to surface-tethered molecules (i.e., ligands). Moreover, because the mass of surface-bound molecules can be quantified, SPR is poised for our intended purpose, except for measuring conformational changes, which is formidable because it requires knowing the dielectric property (i.e., refractive index) of the surface-tethered layer (as governed by its *changing* thickness) (34, 35).

Results

Measuring FG Domain Conformational Changes by SPR. To circumvent the SPR refractive index constraint, we begin with a general expression for the effective refractive index n_{eff} at the interface, which is the weighted sum of local indices (34):

$$n_{\text{eff}} = (2/l_d)\int_0^\infty n(z)\exp(-2z/l_d)dz, \quad [1]$$

where $n(z)$ is the refractive index at height z perpendicular to the sensor surface and l_d is the characteristic evanescent field decay length. For a surface-grafted molecular layer of mean thickness d, $n(z) = n_a$ for $0 \le z \le d$ and $n(z) = n_s$ for $d < z < \infty$ where the subscripts a and s correspond to "adlayer" and "solvent," respectively. Based on this definition, Eq. **1** becomes:

$$n_{\text{eff}} = n_a + (n_s - n_a)\exp(-2d/l_d). \quad [2]$$

In the presence of noninteracting molecules, n_s is replaced by n_p, giving:

$$n_{\text{eff}} = n_a + (n_p - n_a)\exp(-2d/l_d), \quad [3]$$

assuming (*i*) there is a homogeneous distribution of noninteracting molecules in the solvent, and (*ii*) the layer itself is unaffected by the particles (i.e., noninteracting by definition). Subtracting Eqs. **2** and **3** gives:

$$\Delta n_{\text{eff}} = (n_p - n_s)\exp(-2d/l_d), \quad [4]$$

where Δn_{eff} is the change in the effective bulk refractive index (noting that n_a is now eliminated). Further, because the SPR response to changes in the bulk solution refractive index (n) (where $n_{\text{PBS}} = 1.33411$ for PBS and $n_{\text{BSA}} = 1.33567$ for PBS/BSA; *SI Text*) is approximately linear over a restricted range (i.e., $\Delta n = 0.01$) in the absence of adsorption from solution, Δn_{eff} can be replaced by the term R/m (34). Here, R is the SPR response resulting from the noninteracting molecules and m is the slope that relates the change in the SPR response to changes in n. By measuring R and m, Eq. **4** can be solved for the thickness d of a molecular layer:

$$d = \frac{l_d}{2}\ln\left(\frac{m(n_p - n_s)}{R}\right). \quad [5]$$

Now, if a reference cell is implemented in addition to the sample cell (with respective parameters defined by subscripts 1 and 2; *SI Text*), calculating $d_2 - d_1$ gives:

$$d_2 = \frac{l_d}{2}\ln\left(\frac{R_1}{R_2}\frac{m_2}{m_1}\right) + d_1, \quad [6]$$

noting that all the refractive indices are canceled out. Here, d_1 corresponds to a passivation layer of known thickness in the reference cell [i.e., $HS-(CH_2)_{11}-(OCH_2CH_2)_3-OH$ (36); henceforth, $C_{17}H_{36}O_4S$]. We note that Eq. **6** provides the mathematical basis by which the height of a molecular layer can be assessed without the refractive index constraint using $l_d = 350$ nm (*SI Text*). Therefore, any subsequent height change Δd is computed by subtracting the initial layer height given as d_2(initial) from each measured d_2.

Fig. 1 describes the methodology of the assay. First, $C_{17}H_{36}O_4S$ and the cysteine-modified N-terminal FG domain of human Nup62 (amino acids 1–240, 15 FG repeats; henceforth, cNup62) are covalently grafted via thiol binding to cell1 (reference) and cell2 (sample) in the SPR system, respectively. Nonspecific interactions are prevented by filling any exposed gold sites in cell2 with $C_{17}H_{36}O_4S$ (37). R_1 and R_2 are the SPR response signals [in resonance units (RU)] that result from injecting BSA into cell1 and cell2, respectively. BSA molecules are almost entirely excluded from NPCs (38), which makes them ideal as innate molecular probes with minimal external influence on the FG domains. We

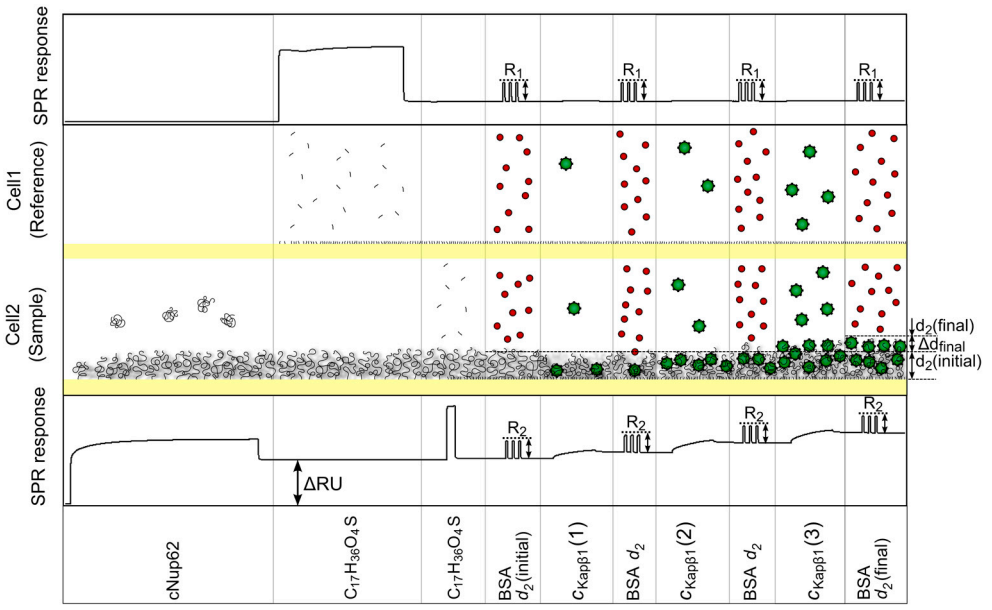

Fig. 1. Measuring binding activity and conformational height changes in situ by SPR. R_1 and R_2 that derive from the presence of innate noninteracting BSA probes (red) in cell 1 ($C_{17}H_{36}O_4S$) and cell 2 (cNup62), respectively, are used to calculate d_2 in Eq. **6**. Stepwise changes Δd that follow Kapβ1 (green) binding are obtained by subtracting d_2(initial) from each d_2. For instance, Δd_{final} corresponds to the overall height difference between d_2(initial) and d_2(final)—i.e., the first and last BSA injections. g_{cNup62} is obtained from the initial shift in the immobilization baseline ΔRU. Likewise, $g_{\text{Kapβ1}}$ and $\rho_{\text{Kapβ1}}$ are obtained from subsequent changes in ΔRU.

further determined that m_2/m_1 is approximately 1, given the negligible difference in SPR sensitivity between cell1 and cell2 (*SI Text*). In accordance with Eq. **6**, d_2(initial) can then be computed for cNup62 using the known value of $d_1 = 2$ nm for the $C_{17}H_{36}O_4S$ layer (36). Moreover, it is useful to correlate d_2 (initial) to the mean cNup62 grafting distance g_{cNup62}, which is estimated from the shift in the immobilization baseline ΔRU as shown in Fig. 1 (39, 40) (i.e., where 1,300 RU = 1 ng/mm^2; *SI Text*). Stepwise height changes Δd in the cNup62 layer can thereafter be obtained by injecting BSA at each respective Kapβ1 concentration ($c_{Kapβ1}$). Likewise, any change in the surface density of bound Kapβ1 ($\rho_{Kapβ1}$) and the mean next-neighbor distance of Kapβ1 ($g_{Kapβ1}$) can be determined from subsequent changes in ΔRU.

Kapβ1-FG Binding Causes a Nonmonotonic Collapse Transition in cNup62. Fig. 2*A* shows a representative SPR measurement where d_2(initial) = 14.1 nm for $g_{cNup62} = 2.4$ nm. Given that d_2(initial) > σ_{cNup62} and $g_{cNup62} < \sigma_{cNup62}$, where σ_{cNup62} (=8.5 nm) is the hydrodynamic size of cNup62, indicates that the FG domains form an extended molecular brush (4). We then calculated Δd, $\rho_{Kapβ1}$, and $g_{Kapβ1}$ for 16 titrations of $c_{Kapβ1}$ increasing from 0.1 nM to 13.4 μM. Striking nonmonotonic phase behavior emerges when Δd is plotted against $\rho_{Kapβ1}$ (Fig. 2*B*): (*1*) Up to $c_{Kapβ1}$ = 40 nM, Δd declines sharply (i.e., negative height change), reaching a minimum at $\rho_{Kapβ1} = 29.9$ Da/nm^2 ($g_{Kapβ1} = 55.5$ nm); (*2*) Δd undergoes a gradual increase that crosses over $\Delta d = 0$ at $\rho_{Kapβ1} = 1{,}010$ Da/nm^2 ($g_{Kapβ1} = 9.8$ nm) when $c_{Kapβ1} = 4$ μM; and (*3*) Δd increases steadily (i.e., positive height change) until $\rho_{Kapβ1} = 1{,}442.6$ Da/nm^2 ($g_{Kapβ1} = 8.2$ nm) at the maximum $c_{Kapβ1} = 13.4$ μM. Further evidence of these transitions can be drawn from correlations with Kapβ1-FG binding activity. In Fig. 2*C*, the quality of a single-component Langmuir isotherm fit (χ^2) to R_{eq} deteriorates once $c_{Kapβ1}$ is increased past 4 μM, where K_D is approximately 400 nM. Conversely, χ^2 is minimized by a two-component fit (*SI Text*) over the entire $c_{Kapβ1}$ range, giving $K_{D1} = 347$ nM and $K_{D2} = 95.9$ μM, which suggests that a low-affinity binding phase emerges at higher $c_{Kapβ1}$ values. For comparison, a single-component fit giving $K_D = 1.28$ μM appropriately describes Kapβ1-FG binding to sparse non–brush-like cNup62 "mushrooms" [Fig. 2*C*, *Inset*; $g_{cNup62} = 11.0$ nm and d_2(initial) = 2.5 nm].

Although Δd accounts for an ensemble average of local height changes, the following qualitative outcomes can be rationalized from *Gedankenexperiment* ("thought experiment"; illustrated in *SI Text*). For phase 1, the following scenarios can be eliminated: (*i*) cNup62 accommodates Kapβ1 ($\Delta d = 0$); (*ii*) cNup62 engulfs Kapβ1 and swells ($\Delta d > 0$); and (*iii*) Kapβ1 stays "perched" on cNup62 ($\Delta d > 0$). As depicted in Fig. 3, the steep negative decline ($\Delta d < 0$) is caused by a local collapse of cNup62 around Kapβ1 due to multivalent Kapβ1-FG interactions. In phase 2, the "recovery" in Δd is a consequence of in-layer steric crowding as caused by a further addition of Kapβ1, which rearranges the FG domains into more entropy-favoring conformations. Subsequent cross-over occurs ($\Delta d \to 0$; $c_{Kapβ1} = 4$ μM) when $\rho_{Kapβ1}$ = 1,010 Da/nm^2, which closely approximates the expected surface density of a packed Kapβ1 monolayer (approximately 1,000 Da/nm^2) [from small angle X-ray scattering data (41); *SI Text*]. Referring to Fig. 2*C*, $K_{D1} = 347$ nM is relatively strong up until this point owing to maximal Kapβ1-FG binding within the cNup62 layer. However, correlating $\Delta d > 0$ and K_{D2} = 95.9 μM in phase 3 indicates the formation of a weakly bound secondary "pileup" layer when excess Kapβ1 binds to unoccupied FG domain regions that protrude from the cNup62 layer.

In Fig. 4*A*, the results of Δd vs. $\rho_{Kapβ1}$ obtained from cNup62 brushes with different g_{cNup62} and d_2(initial) indicate that the collapse transition is a common feature during initial Kapβ1 binding. This is followed by a recovery phase with taller brushes

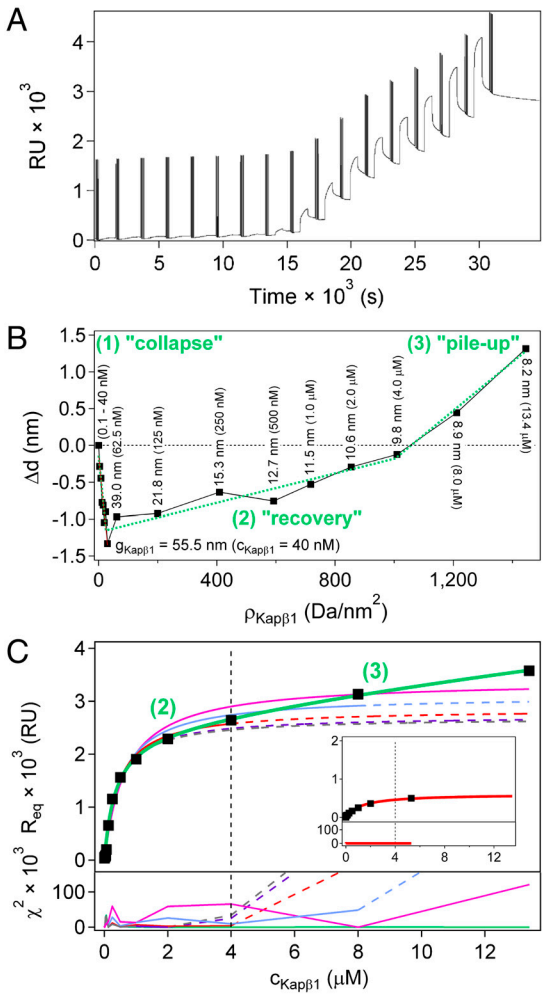

Fig. 2. Nonmonotonic behavior in a cNup62 brush caused by Kapβ1-FG binding. (*A*) Successive 3 · 30 s BSA injections follow 16 $c_{Kapβ1}$ titrations ranging from 0.1 nM to 13.4 μM on a cNup62 brush characterized by g_{cNup62} = 2.4 nm and d_2(initial) = 14.1 nm. (*B*) The cNup62 brush undergoes collapse at low $\rho_{Kapβ1}$ (*1*), followed by recovery (*2*), which reaches pileup (*3*) upon crossing Δd equal 0. Included are the values of $g_{Kapβ1}$ and $c_{Kapβ1}$ (in parentheses) that correspond to each respective Δd measurement. (*C*) The steady-state (R_{eq}) SPR response across the entire $c_{Kapβ1}$ range (from *A*; 0.1 nM to 13.4 μM) is optimally fit using a two-component Langmuir isotherm (green) giving $K_{D1} = 347$ nM and $K_{D2} = 95.9$ μM. For single fits (K_D of approximately 400 nM), χ^2 is minimized at low terminal $c_{Kapβ1}$ values (grey, purple, and red) but deviates past $c_{Kapβ1} > 4$ μM (blue and pink). Solid and dashed lines denote the actual fitted $c_{Kapβ1}$ range and the predicted K_D behavior, respectively. (*Inset*) A single $K_D = 1.28$ μM is found for Kapβ1 binding to sparse cNup62 mushrooms where $g_{cNup62} = 11.0$ nm and d_2(initial) = 2.5 nm.

requiring more Kapβ1 molecules (higher $\rho_{Kapβ1}$) to reach pileup. Recalling that $\rho_{Kapβ1}$ for a Kapβ1 monolayer is approximately 1,000 Da/nm^2 indicates that taller brushes [d_2(initial) > 14.1 nm] accommodate a secondary Kapβ1 layer to recover. For comparison, sparser mushroom-like cNup62 layers undergo a negligible collapse and reach pileup without recovering. A three-dimensional spatial description is shown in Fig. 4*B*, where the change in total mass-volume density $\Delta\upsilon$ (i.e., cNup62 and Kapβ1) is plotted against relative height change $\Delta d/d_2$(initial). During collapse, the linear increase in $\Delta\upsilon$ is dominated by a compaction of cNup62 because only small amounts of Kapβ1 are bound. Interestingly, the overlap indicates that $\Delta\upsilon$ scales with $\Delta d/d_2$(initial), that is, the total amount of space occupied is equally optimized within different cNup62 layers regardless of their initial brush conformation or amount of bound Kapβ1. During the initial stages of recovery, $\Delta\upsilon$ increases at constant $\Delta d/d_2$(initial) where the void

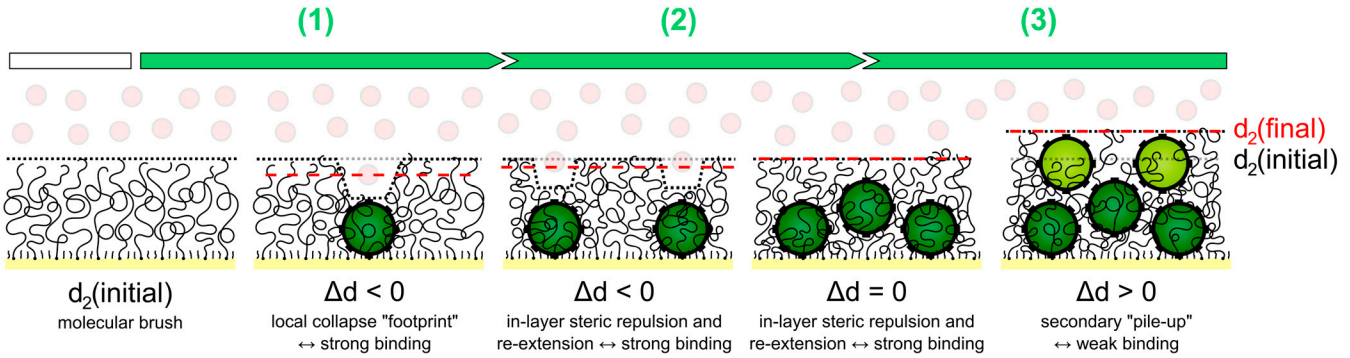

Fig. 3. Kapβ1-FG binding activity and cNup62 form–function are intimately coupled. (*1*) A local collapse of cNup62 occurs around Kapβ1 owing to strong multivalent Kapβ1-FG (dark green) binding at low $\rho_{Kap\beta1}$. (*2*) Additional Kapβ1 molecules bind tightly in the cNup62 layer, driving unoccupied FG domains to extend or recover because of increasing in-layer steric repulsion whereupon the layer self-heals, reaching $\Delta d = 0$. (*3*) At high $\rho_{Kap\beta1}$, a secondary layer of Kapβ1 (light green) binds weakly to unoccupied FG domain protrusions giving $\Delta d > 0$. Red dashed lines correspond to the cNup62 layer height as measured by BSA (red watermarked).

volume of each layer is being filled with additional Kapβ1. Upon reaching pileup, $\Delta\upsilon$ approaches a saturated critical capacity that is maintained by increasing $\Delta d/d_2(\text{initial})$ (i.e., via FG domain rearrangements). While our interpretation is consistent with theoretical predictions (42), we note that pileup commences sooner for sparse cNup62 layers because of their isolation and lower capacity to bind Kapβ1.

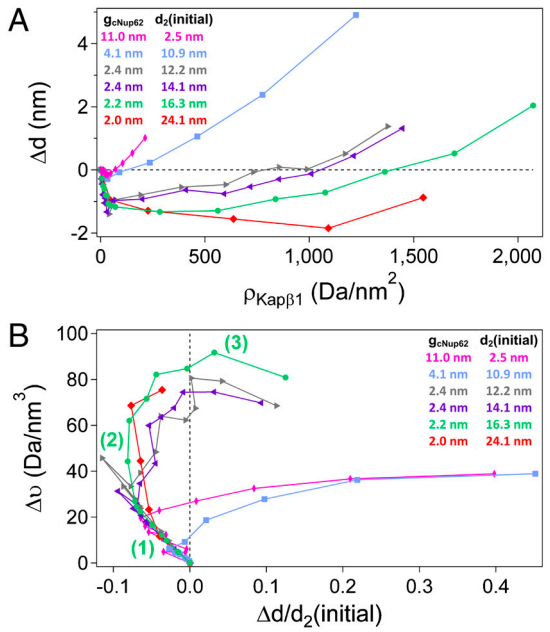

Fig. 4. Brushes collapse sparse layers do not. (*A*) Plot of Δd vs. $\rho_{Kap\beta1}$, where the extent of collapse increases for taller cNup62 brushes (red > green > purple > grey) as compared to sparser layers (blue, pink). A greater amount of bound Kapβ1 is also required for taller brushes to recover before reaching pileup (red > green > purple > grey). Sparse cNup62 layers exhibit a negligible collapse followed by an immediate pileup without recovering (blue, pink). (*B*) Plot of the total (Kapβ1 and cNup62) mass-volume density change $\Delta\upsilon$ vs. relative height change $\Delta d/d_2(\text{initial})$. (*1*) For brushes (red, green, purple, grey), a linear increase in $\Delta\upsilon$ accompanies a 10% reduction in $\Delta d/d_2(\text{initial})$ because of cNup62 compaction upon collapse. Their overlap reveals that the total space occupied scales with the extent of collapse and is conserved. (*2*) The transition into recovery at $\Delta\upsilon$ of approximately 20 Da/nm^3 proceeds with additional Kapβ1 binding without changing $\Delta d/d_2(\text{initial})$. Saturation at $\Delta\upsilon$ of approximately 70 Da/nm^3 denotes FG domain reextension to maintain its capacity to accommodate more Kapβ1, marking the commencement of (*3*) pileup. Sparser conformations (blue, pink) have a low Kapβ1 capacity, and pile up at low $\Delta\upsilon$ without recovering.

Kapβ1-FG Binding Avidity Depends on cNup62 Conformation. Fig. 5*A* summarizes the dependence of $d_2(\text{initial})$ on g_{cNup62}. Clearly, extended molecular brushes form at small g_{cNup62}, and transition into sparser layers or mushrooms at large g_{cNup62}. Because cNup62 (pI = 9.31) is net positively charged at pH 7.2, we deduce that this behavior is polyelectrolytic in nature (i.e., forming polyelectrolyte brushes), as suggested by Flory–Huggins theory (43) (*SI Text*). The corresponding plot of K_D vs. g_{cNup62} in Fig. 5*B* reveals how nonmonotonic behavior is linked to Kapβ1-FG binding avidity. When $g_{cNup62} > \sigma_{cNup62}$, single K_D values of approximately 10 μM reflect the limited propensity of individual cNup62 mushrooms to bind Kapβ1. This appears to split at $g_{cNup62} < \sigma_{cNup62}$, where two binding constants (K_{D1} and K_{D2}) emerge becoming more apparent at low g_{cNup62} (Fig. 2*C*) because of the onset of brush formation. At low to moderate $c_{Kap\beta1}$, strong binding (K_{D1} of approximately 0.2 μM) accompanies collapse and recovery where Kapβ1 has access to FG repeats residing amongst neighboring FG domains, thereby reaching a maximum (K_{D1} decreases) at small g_{cNup62}. This is consistent with prevailing sub-μM K_D values, noting that the highest Kap concentrations tested were below 1 μM (27–29). At large $c_{Kap\beta1}$, however, in-layer steric crowding and a reduction of unoccupied FG repeats give rise to weaker binding (K_{D2} ranging from 10 μM to 1 mM) that is associated with pileup. The large variation in K_D is therefore a hallmark of binding avidity that emerges from the myriad of Kapβ1-FG binding possibilities that derive from the inherent flexibility and conformational susceptibility of surface-tethered FG domains.

Discussion

We have shown that self-healing nonmonotonic FG domain behavior is intimately coupled to Kapβ1-FG binding activity as defined by their relative spatial arrangements (i.e., g_{cNup62} and $g_{Kap\beta1}$). This results from a competition between FG domain collapse (caused by multivalent Kapβ1-FG binding) and FG domain reextension, which maximizes the capacity of the layer to bind more Kapβ1. Supposing that only sparse FG domain mushrooms existed in the pore, one might expect an increase in passive transport owing to a reduction in barrier functionality; counterintuitively, however, selective transport could slow down because of a comparatively high Kapβ1-FG binding affinity (K_D of approximately 10 μM; Fig. 5*B*). Instead, our findings support a view where crowding is not only important for selectivity (44), but also essential for promoting fast Kapβ1 transport in the NPC (45). Indeed, the high FG domain surface density (small g_{cNup62}) data, which bears a close resemblance to the NPC (where up to 128 copies of Nup62 may be present; ref. 46), predicts that at least two Kapβ1 binding phases exist at physiological concentrations ($c_{Kap\beta1}$ of approximately 10 μM; ref. 47): (*i*) strong binding (K_{D1}) amongst

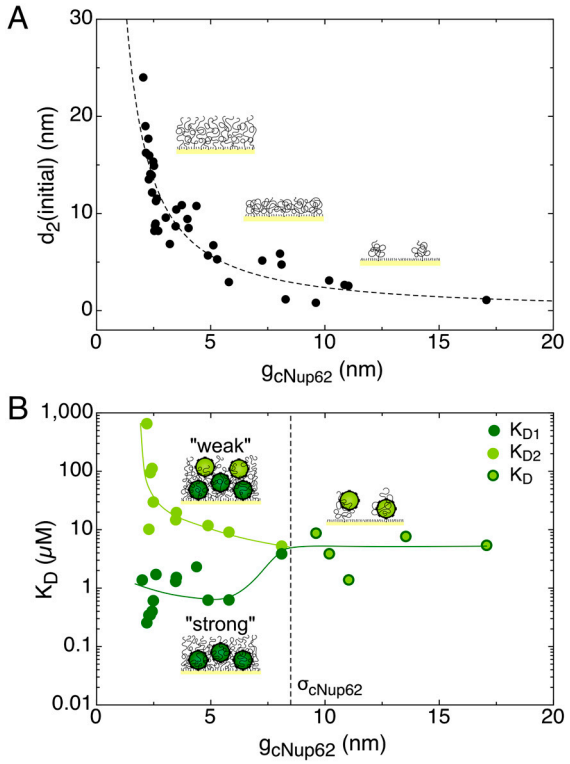

Fig. 5. Brush height and Kapβ1 binding avidity are correlated via cNup62 grafting distance. (*A*) Dependence of d_2(initial) on g_{cNup62}, showing that cNup62 forms a molecular brush at low g_{cNup62} (i.e., high surface grafting density) and transitions towards sparse mushrooms at high g_{cNup62}. A fit of the Flory–Huggins equation to d_2(initial) suggests that cNup62 is polyelectrolytic in nature (*SI Text*). (*B*) Kapβ1 binding affinity to cNup62 is modulated by g_{cNup62}. An intermediate single binding phase occurs at g_{cNup62} larger than σ_{cNup62} (=8.5 nm; dotted line) because of the limited Kapβ1 binding capacity of sparse mushrooms. This splits at low g_{cNup62} (i.e., in the brush regime), where strong binding to cNup62 (K_{D1}; dark green) occurs at low to moderate $c_{Kapβ1}$ (collapse and recovery), whereas weak binding (K_{D2}; light green) occurs at large $c_{Kapβ1}$ (pileup).

a population of semicollapsed FG domains at the pore walls; and (*ii*) weak Kapβ1 binding (K_{D2}) to unoccupied FG domain protrusions near the pore center. As follows, it is the weak binding phase in a Kapβ1-crowded pore that is key to promoting fast transport rates.

Altogether this is reminiscent of a "highway" effect, where Kap transport is slow at the pore walls but fast near the pore center (Fig. 6) as can be inferred from two-phase binding in NPC transport studies (48). More striking evidence can be found from the single molecule fluorescence studies of Ma et al. in terms of the preferred location of Kapβ1 along the NPC walls that leaves a narrow passage at the pore center for passive diffusion to proceed (49). The transition from more collapsed FG domain segments nearer the walls to unoccupied protrusions toward the center may certainly contribute to the inhomogeneous, viscous characteristics of the central channel (50). Nevertheless, understanding the collective FG domain response in the NPC will require an evaluation of the surface density for each different FG Nup and the effects of Kapβ1 binding avidity. The highway effect might also explain how increasing $c_{Kapβ1}$ sharply decreases NPC interaction time, thereby improving import efficiency (45). Without precluding the effect of weakly binding competitors (30), this might explain how in vivo NPC transport is fast despite strong binding avidity in vitro. It is noteworthy that the K_{D2} measurements lie in close agreement with the range of weak μM to mM affinities anticipated to describe known NPC transport rates (i.e.,

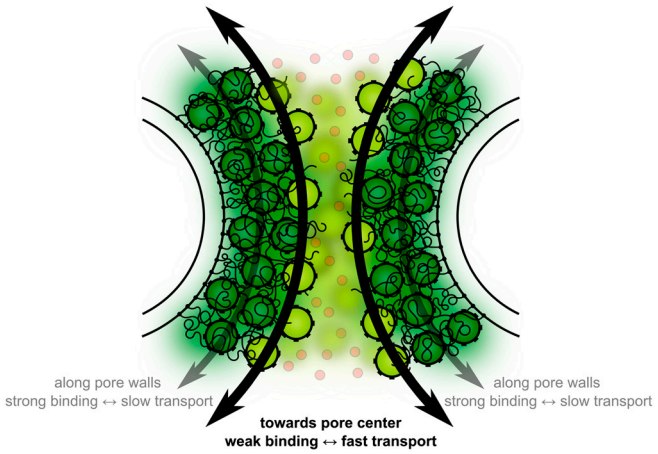

Fig. 6. The NPC transport highway where Kapβ1 traffic can proceed via at least two "lanes" at physiological concentrations. Slow transport is anticipated for strongly bound Kapβ1 molecules (dark green) that saturate semicollapsed FG domains around the pore walls. Fast transport occurs nearer the pore center, where Kapβ1 binds weakly to unoccupied FG domain protrusions (light green). Small passive molecules (red watermarked) may diffuse freely through the pore center.

approximately 10 ms) (30). Thus, binding avidity need not hinder fast transport per se.

Finally, our findings reconcile the key features postulated by different NPC models. While entropic exclusion rejects nonbinding molecules (4, 24), nonmonotonic behavior signifies that the FG domains are not permanently collapsed but undergo dynamic rearrangements during Kapβ1 transport (6). Importantly, this imparts a self-healing mechanism on surface-tethered FG domains in the NPC at the nanometer scale without requiring for hydrophobic FG cross-linking as argued from the basis of bulk FG hydrogels that take over several micrometers to reseal (8). Hence, one may consider the population of strongly bound Kapβ1 as integral constituents of the NPC (25). Nevertheless, the occurrence of the weak binding phase does bring into question the role of RanGTP in dissociating Kapβ1 from the FG domains (18). To clarify, we have also ascertained that Kapβ1 does not bind covalently to the underlying gold SPR surface (*SI Text*), thereby disputing allegations (10) that the FG domain collapse constitutes an in vitro artifact. Methodological differences aside, the mismatch in Kapβ1 concentrations may explain why FG domain collapse was observed for Nup153 brushes ($c_{Kapβ1} \leq 33$ nM) (6), but not for brushes of Nsp1 ($c_{Kapβ1} \geq 200$ nM) (10). In the future, experimentation ought to involve stepwise height measurements spanning from low-nM to approximately 10 μM Kapβ1 concentrations. On a related note, it should be instructive that Kap binding activity cannot be rationalized (10) from conformational FG domain behavior alone.

To conclude, we have uncovered Kapβ1-FG domain behavior that reconciles transport and mechanistic aspects of NPC functionality. Such insight can contribute to the functional design and optimization of biomimetic selective channels and nanopores (9, 11, 51). On a technical note, our SPR methodology affords the correlation of binding affinities, in-plane molecular arrangements, and conformational changes in situ. This can be powerful in resolving the form–function relationships of diverse surface-tethered IDPs (52–54) and other stimuli-responsive polymers (55, 56) on biological interfaces.

Methods

Cloning and Expression of Recombinant cNup62 and Kapβ1. A comprehensive description of the following protocols can be found in ref. 11. Briefly, the N-terminal FG repeat domain of human Nup62 (amino acids 1–240) was subcloned by GenScript Inc. into pPEP-TEV vector at the BamHI and SalI restriction sites. One cysteine was added to its C terminus (Cys-Nup62) as a covalent tether to Au. The recombinant N-terminal His_6-tagged cNup62

and Kapβ1 were expressed in *Escherichia coli* BL21 (DE3) cells. The final protein purity was analyzed by SDS/PAGE (*SI Text*), and selected fractions were dialyzed against PBS (pH 7.2; Invitrogen) for further use.

Other Materials. Ten mg/mL BSA (Sigma–Aldrich) was carefully dissolved in PBS; $C_{17}H_{36}O_4S$ (Nanoscience) was dissolved until reaching 10 mM in ethanol and diluted with PBS to 1 mM before experimentation.

SPR Sensor Chip Preparation. SPR bare gold sensor chips (SIA Kit Au) were from GE Healthcare. Upon removal from storage in an argon atmosphere, gold sensor surfaces were ultrasonicated in acetone and high-purity ethanol (Merck) for 15 min, respectively, and dried in a nitrogen gas stream followed by 60 min UVO cleaning (Model 42A-220; Jelight Company Inc.). The gold sensor surfaces were then ultrasonicated for another 15 min in ethanol, dried in a nitrogen gas stream, and mounted on the sample holder for immediate SPR usage. A comprehensive description of the SPR measurement protocol with error analysis can be found in *SI Text*.

Dynamic Light Scattering. Hydrodynamic diameter measurements of Kapβ1 and cNup62 were made in PBS with the addition of 1 mM DTT using a Zetasizer Nano instrument (Malvern). This gave $\sigma_h = 8.47 \pm 0.45$ nm (polydispersity index $= 0.36 \pm 0.08$) for cNup62 and $\sigma_h = 12.06 \pm 2.09$ nm (polydispersity index $= 0.423 \pm 0.19$) for Kapβ1, using $n = 1.45$ and $n = 1.330$ as the refractive index for proteins and dispersant [i.e., water; $t = 25.0$ °C, viscosity $=$ 0.8872 cP ($1P = 0.1$ Pa•s)], respectively.

ACKNOWLEDGMENTS. We thank A. Zilman for helpful discussions. This work is supported by the National Center of Competence in Research "Nanoscale Science" and the Swiss National Science Foundation.

1. Tompa P (2010) *Structure and Function of Intrinsically Disordered Proteins* (CRC, Boca Raton, FL).
2. Uversky VN, Dunker AK (2012) Multiparametric analysis of intrinsically disordered proteins: Looking at intrinsic disorder through compound eyes. *Anal Chem* 84:2096–2104.
3. Gray JJ (2004) The interaction of proteins with solid surfaces. *Curr Opin Struct Biol* 14:110–115.
4. Lim RYH, et al. (2006) Flexible phenylalanine-glycine nucleoporins as entropic barriers to nucleocytoplasmic transport. *Proc Natl Acad Sci USA* 103:9512–9517.
5. Frey S, Gorlich D (2007) A saturated FG-repeat hydrogel can reproduce the permeability properties of nuclear pore complexes. *Cell* 130:512–523.
6. Lim RYH, et al. (2007) Nanomechanical basis of selective gating by the nuclear pore complex. *Science* 318:640–643.
7. Patel SS, Belmont BJ, Sante JM, Rexach MF (2007) Natively unfolded nucleoporins gate protein diffusion across the nuclear pore complex. *Cell* 129:83–96.
8. Frey S, Gorlich D (2009) FG/FxFG as well as GLFG repeats form a selective permeability barrier with self-healing properties. *EMBO J* 28:2554–2567.
9. Jovanovic-Talisman T, et al. (2009) Artificial nanopores that mimic the transport selectivity of the nuclear pore complex. *Nature* 457:1023–1027.
10. Eisele NB, Frey S, Piehler J, Gorlich D, Richter RP (2010) Ultrathin nucleoporin phenylalanine-glycine repeat films and their interaction with nuclear transport receptors. *EMBO Rep* 11:366–372.
11. Kowalczyk SW, et al. (2011) Single-molecule transport across an individual biomimetic nuclear pore complex. *Nat Nanotechnol* 6:433–438.
12. Denning DP, Patel SS, Uversky V, Fink AL, Rexach M (2003) Disorder in the nuclear pore complex: The FG repeat regions of nucleoporins are natively unfolded. *Proc Natl Acad Sci USA* 100:2450–2455.
13. Cronshaw JA, Krutchinsky AN, Zhang WZ, Chait BT, Matunis MJ (2002) Proteomic analysis of the mammalian nuclear pore complex. *J Cell Biol* 158:915–927.
14. Alber F, et al. (2007) The molecular architecture of the nuclear pore complex. *Nature* 450:695–701.
15. Stewart M (2007) Molecular mechanism of the nuclear protein import cycle. *Nat Rev Mol Cell Biol* 8:195–208.
16. Grunwald D, Singer RH, Rout M (2011) Nuclear export dynamics of RNA-protein complexes. *Nature* 475:333–341.
17. Yang W (2011) 'Natively unfolded' nucleoporins in nucleocytoplasmic transport. *Nucleus* 2:10–16.
18. Lyman SK, Guan TL, Bednenko J, Wodrich H, Gerace L (2002) Influence of cargo size on Ran and energy requirements for nuclear protein import. *J Cell Biol* 159:55–67.
19. Bayliss R, Littlewood T, Stewart M (2000) Structural basis for the interaction between FxFG nucleoporin repeats and importin-beta in nuclear trafficking. *Cell* 102:99–108.
20. Isgro TA, Schulten K (2005) Binding dynamics of isolated nucleoporin repeat regions to importin-beta. *Structure* 13:1869–1879.
21. Peleg O, Lim RYH (2010) Converging on the function of intrinsically disordered nucleoporins in the nuclear pore complex. *Biol Chem* 391:719–730.
22. Paine PL, Moore LC, Horowitz SB (1975) Nuclear-envelope permeability. *Nature* 254:109–114.
23. Hoelz A, Debler EW, Blobel G (2011) The structure of the nuclear pore complex. *Annu Rev Biochem* 80:613–643.
24. Rout MP, et al. (2000) The yeast nuclear pore complex: Composition, architecture, and transport mechanism. *J Cell Biol* 148:635–651.
25. Peters R (2009) Translocation through the nuclear pore: Kaps pave the way. *Bioessays* 31:466–477.
26. Yamada J, et al. (2010) A bimodal distribution of two distinct categories of intrinsically disordered structures with separate functions in FG nucleoporins. *Mol Cell Proteomics* 9:2205–2224.
27. Ben-Efraim I, Gerace L (2001) Gradient of increasing affinity of importin beta for nucleoporins along the pathway of nuclear import. *J Cell Biol* 152:411–417.
28. Bednenko J, Cingolani G, Gerace L (2003) Importin beta contains a COOH-terminal nucleoporin binding region important for nuclear transport. *J Cell Biol* 162:391–401.
29. Lott K, Bhardwaj A, Mitrousis G, Pante N, Cingolani G (2010) The importin beta binding domain modulates the avidity of importin beta for the nuclear pore complex. *J Biol Chem* 285:13769–13780.
30. Tetenbaum-Novatt J, Hough LE, Mironska R, McKenney AS, Rout MP (2012) Nucleocytoplasmic transport: A role for non-specific competition in karyopherin-nucleoporin interactions. *Mol Cell Proteomics* 11:31–46.
31. Schuck P (1997) Use of surface plasmon resonance to probe the equilibrium and dynamic aspects of interactions between biological macromolecules. *Annu Rev Biophys Biomol Struct* 26:541–566.
32. Knoll W (1998) Interfaces and thin films as seen by bound electromagnetic waves. *Annu Rev Phys Chem* 49:569–638.
33. Homola J (2008) Surface plasmon resonance sensors for detection of chemical and biological species. *Chem Rev* 108:462–493.
34. Jung LS, Campbell CT, Chinowsky TM, Mar MN, Yee SS (1998) Quantitative interpretation of the response of surface plasmon resonance sensors to adsorbed films. *Langmuir* 14:5636–5648.
35. Koutsioubas AG, Spiliopoulos N, Anastassopoulos DL, Vradis AA, Priftis GD (2007) Surface plasmon resonance as a tool for the estimation of adsorbed polymeric layer characteristics: Theoretical considerations and experiment. *J Polymer Sci B Polymer Phys* 45:2060–2070.
36. Palegrosdemange C, Simon ES, Prime KL, Whitesides GM (1991) Formation of self-assembled monoloayers by chemisorption of derivatives of oligo(ethylene glycol) of structure HS(CH2)11(OCH2CH2)META-OH on gold. *J Am Chem Soc* 113:12–20.
37. Levicky R, Herne TM, Tarlov MJ, Satija SK (1998) Using self-assembly to control the structure of DNA monolayers on gold: A neutron reflectivity study. *J Am Chem Soc* 120:9787–9792.
38. Ribbeck K, Gorlich D (2001) Kinetic analysis of translocation through nuclear pore complexes. *EMBO J* 20:1320–1330.
39. Lofas S, et al. (1991) Bioanalysis with surface plasmon resonance. *Sensor Actuator B* 5:79–84.
40. Stenberg E, Persson B, Roos H, Urbaniczky C (1991) Quantitative determination of surface concentration of protein with surface plasmon resonance using radiolabeled proteins. *J Colloid Interface Sci* 143:513–526.
41. Forwood JK, et al. (2010) Quantitative structural analysis of importin-beta flexibility: Paradigm for Solenoid protein structures. *Structure* 18:1171–1183.
42. Kim JU, O'Shaughnessy B (2002) Morphology selection of nanoparticle dispersions by polymer media. *Phys Rev Lett* 89:238301.
43. Bright JN, Woolf TB, Hoh JH (2001) Predicting properties of intrinsically unstructured proteins. *Prog Biophys Mol Biol* 76:131–173.
44. Zilman A, Di Talia S, Chait BT, Rout MP, Magnasco MO (2007) Efficiency, selectivity, and robustness of nucleocytoplasmic transport. *PLoS Comput Biol* 3:1281–1290.
45. Yang WD, Musser SM (2006) Nuclear import time and transport efficiency depend on importin beta concentration. *J Cell Biol* 174:951–961.
46. Solmaz SR, Chauhan R, Blobel G, Melcak I (2011) Molecular architecture of the transport channel of the nuclear pore complex. *Cell* 147:590–602.
47. Paradise A, Levin MK, Korza G, Carson JH (2007) Significant proportions of nuclear transport proteins with reduced intracellular mobilities resolved by fluorescence correlation spectroscopy. *J Mol Biol* 365:50–65.
48. Tokunaga M, Imamoto N, Sakata-Sogawa K (2008) Highly inclined thin illumination enables clear single-molecule imaging in cells. *Nat Methods* 5:159–161.
49. Ma J, Yang W (2010) Three-dimensional distribution of transient interactions in the nuclear pore complex obtained from single-molecule snapshots. *Proc Natl Acad Sci USA* 107:7305–7310.
50. Ma J, Goryaynov A, Sarma A, Yang W (2012) Self-regulated viscous channel in the nuclear pore complex. *Proc Natl Acad Sci USA* 109:7326–7331.
51. Caspi Y, Zbaida D, Cohen H, Elbaum M (2008) Synthetic mimic of selective transport through the nuclear pore complex. *Nano Lett* 8:3728–3734.
52. Dunker AK, Brown CJ, Lawson JD, Iakoucheva LM, Obradovic Z (2002) Intrinsic disorder and protein function. *Biochemistry* 41:6573–6582.
53. Dyson HJ, Wright PE (2005) Intrinsically unstructured proteins and their functions. *Nat Rev Mol Cell Biol* 6:197–208.
54. Srinivasan N, Kumar S (2012) Ordered and disordered proteins as nanomaterial building blocks. *Wiley Interdiscip Rev Nanomed Nanobiotechnol* 4:204–218.
55. Nel AE, et al. (2009) Understanding biophysicochemical interactions at the nano-bio interface. *Nat Mater* 8:543–557.
56. Stuart MAC, et al. (2010) Emerging applications of stimuli-responsive polymer materials. *Nat Mater* 9:101–113.